J Mater Sci: Mater Electron **(2025) 36:1204**

Revival of quantum confinement effect and stabilization of tetragonal phase in TiO_2 Nanopowders with annealing temperature

E. Asikuzun Tokeser[1], U. Esturk[2], S. Kurnaz[3], and O. Ozturk[4,*]

[1] *Department of Metallurgical and Materials Engineering, Faculty of Engineering and Architecture, Kastamonu University, Kastamonu 37200, Turkey*
[2] *Department of Materials Science and Engineering, Institute of Science, Kastamonu University, Kastamonu 37200, Turkey*
[3] *Research and Application Center, Kastamonu University, 37200 Kastamonu, Turkey*
[4] *Department of Electrical and Electronics Engineering, Faculty of Engineering and Architecture, Kastamonu University, Kastamonu 37200, Turkey*

Received: 7 March 2025
Accepted: 27 June 2025
Published online: 10 July 2025

ABSTRACT

This research is concerned with the variations of mechanical, structural, physical, and magnetic properties of titanium dioxide (TiO_2) nanopowders produced via sol–gel method with annealing temperatures intervals 300 to 1100 °C. The effects of the phase transitions on the main chracteristics of TiO_2 nanopowders are exstensively analyzed using X-ray diffraction (XRD), scanning electron microscopy (SEM), vibrating sample magnetometry (VSM), and Vickers microhardness (H_v) measurements. XRD investigations reveal an amorphous crystal structure at lower annealing temperatures (300–400 °C), followed by the formation of the chracteristic anatase phase (450–500 °C), and finally the transition to the rutile phase (600–1100 °C). All TiO_2 nanopowders exhibit a tetragonal crystal structure. The avarage grain size parameter is found to increase depending on the lattice strain relaxation while dislocation density decreases regularly with the increase in the annealing temperature. Further, SEM images show that increasing calcination temperature improves crystallization quality due to increased agglomeration along intergrain boundaries and promotes the formation of a more spherical morphology. Accordingly, the heat energy serving as the driving force for the reordering of skeleton develops the crystallization system and grain boundary couplings in the TiO_2 main matrix. Namely, the quantum confinement effect is clearly observed with the temperature gradient in the TiO_2 nanometer scale materials produced in this work. Additionally, VSM measurements indicate ferromagnetic behavior in all samples, and magnetic saturation is achieved at 1.5 Tesla. The hardness results indicate that the H_v values are found to enhance regularly with increasing annealing temperature as a consequence of degradation of interparticle bonds, non-uniform grain orientation distributions, reduced contact points

Address correspondence to E-mail: oozturk@kastamonu.edu.tr

https://doi.org/10.1007/s10854-025-15283-z

between semiconductor particles, and the potential formation of impurity phases. The improvement stems from the phase transformation from anatase-to-rutile. Besides, all the semiconducting nanopowders produced exhibit standard the indentation size effect behavior. The experimental load-indepenendet hardness results in the saturation limit regions are compared with semi-empirical mechanical models. It is observed that the Hays-Kendall (HK) approach demonstrates the most accurate prediction of real microhardness values.

1 Introduction

Titanium dioxide (TiO_2) is a versatile transition metal oxide semiconductor renowned for its exceptional properties including non-toxicity, cost-effectiveness, stability, ease of handling, biocompatibility, high product homogeneity, low processing temperature, efficiency, and resistance to photochemical and chemical degradation [1–3]. In this resepct, the TiO_2 structures is an attractive material for various applications such as solar cells [4], chemical sensors [5], self-cleaning surfaces [6], photocatalyst [7], and environmental treatment technologies [1]. The non-toxic nature of TiO_2, coupled with its biocompatibility, has led to its extensive use in biomedical applications including drug delivery and tissue engineering [8]. Additionally, the low cost and abundance of titanium make TiO_2 an economically viable option for large-scale production and industrial applications [9]. The structural stability of TiO_2 material (particularly resistance to photocorrosion and chemical degradation) is crucial for its long-term performance in various environments [10]. Besides, the stability ensures the sustained functionality of TiO_2-based devices and coatings, making the material a reliable choice for outdoor and harsh-condition applications [11]. Moreover, the ease of handling and processing TiO_2 facilitates the integration into various manufacturing processes, further expanding the potential applications of the compound in diverse fields [12]. For instance, TiO_2 nanoparticles can readily be synthesized and incorporated into coatings, films, and composites, enabling the development of advanced materials with tailored properties [13].

TiO_2 exists in both amorphous and crystalline states, with the latter predominantly occurring in three polymorphs such as anatase, rutile, and brookite. Anatase and rutile share a tetragonal crystal structure while brookite possesses an orthorhombic unit cell. Among these polymorphs, rutile is the most thermodynamically stable phase. On the other hand, anatase and brookite phases are metastable and undergo a phase transition to rutile upon heating [14, 15]. TiO_2 synthesis encompasses a variety of methods including conventional solid-state reactions, precipitation, hydrothermal, microwave hydrothermal, solvothermal, and sol–gel techniques [16]. Amongst, the latter preparation method stands out for its ability to produce high-quality powders with exceptional purity, homogeneity, and finer particle size [17]. In the sol–gel process, the reaction between organometallic precursors and water initiates two simultaneous reactions: hydrolysis and condensation [18]. The reactions are highly sensitive to experimental parameters such as feed concentration, hydrolysis temperature, pH, and mixing conditions [19]. The hydrolysis reaction generates the initial nuclei or basic titanium dioxide units, while the condensation reaction facilitates the growth of the basic units [20]. Notably, the powders obtained in this study consist of a mixture of amorphous TiO_2 with anatase, and rutile phases [21]. The sol–gel method also offers several advantages over other synthesis techniques. Firstly, it allows for precise control over the composition and properties of the resulting TiO_2 powders by adjusting the experimental parameters [22]. Secondly, the low processing temperature ranges of the sol–gel method prevent the agglomeration of particles, leading to a higher surface area and enhanced reactivity [23]. Finally, the versatility of the sol–gel process enables the synthesis of TiO_2 in various forms including nanoparticles, thin films, and aerogels [24]. However, the sol–gel method also presents some challenges. The hydrolysis and condensation reactions are highly sensitive to moisture and other environmental factors, requiring meticulous control over the

reaction conditions [25]. Additionally, the removal of organic residues from the final product can be a complex and time-consuming process [26]. Despite the challenges mentioned, the sol–gel method remains a popular and effective technique for synthesizing high-quality TiO_2 powders with tailored properties. That is exactly why ongoing research focuses on optimizing the sol–gel process to overcome its limitations and further enhance the quality and functionality of TiO_2 materials.

During the annealing process, a critical first-order phase transition occurs when transforming the metastable anatase and brookite phases into the thermodynamically stable rutile phase. The transition pathways can be multifaceted, including direct anatase-to-rutile transformation, as well as more complex routes such as anatase → brookite → rutile and brookite → anatase → rutile. The specific conditions governing the transformation mechanisms are influenced by various factors, viz. annealing temperature, particle size, and substrate types [27]. Of the factors, annealing temperature is paramount, as it dictates the kinetics and thermodynamics of the phase transitions. Depending on the specific combination of the parameters, the anatase phase can transform the rutile phase at temperatures ranging from 400 to 1000 °C [28, 29]. Understanding and controlling the phase transitions are of critical importance in tailoring the fundameantal chracteristics of TiO_2 materials for specific application fields. For instance, The photocatalytic activity of TiO_2 structure depends largely on its crystal structure, and anatase phase generally shows superior photocatalytic performance as compared to that of rutile phase [30, 31]. Therefore, precise control over the annealing conditions is essential to obtain the desired phase composition and optimize the characteristic material properties for its intended use. It is well-knwon that the precise control stems from the intricate relationship between TiO_2's physical and chemical properties and its atomic-level surface structure, a relationship that has driven significant advancements in surface science. TiO_2, as a metal oxide, possesses both ionic and covalent bonds, contributing to its unique surface chemistry compared to other metals and semiconductors. Extensive research has revealed the distinctive crystalline structure and metal oxide surface of TiO_2 structure. Notably, the polymorphic structure of TiO_2 crystals is heavily influenced by the synthesis method employed, with different synthesis routes leading to variations in phase development and particle size growth. The sol–gel method, for example, allows for greater control over particle size and morphology compared to other methods like solid-state reactions.

The study of TiO_2 nanopowders and thin films is of increasing significance due to their potential applications in various technological fields. In the current investigation, we focus on elucidating the effects of annealing temperature on the phase transformations and general chracteristic features of TiO_2 nanopowders synthesized via the sol–gel method. On this basis, a key objective of this research is to systematically investigate the phase evolution of TiO_2 nanopowders as a function of annealing temperature. By subjecting the sol–gel-derived TiO_2 to a range of temperatures, we aim to induce and characterize the transitions between amorphous, anatase, and rutile phases. Moreover, the variation in the crysta structure, surface morphology apprance, and fundamnetal magnetic performance features belonging to the TiO_2 system based on the annealig temperatures is extensively investigated. The comprehensive analyses will provide valuable insights into the thermodynamic and kinetic aspects governing the phase stability of TiO_2 nanopowders. Furthermore, we recognize the scarcity of studies focusing on the mechanical characterization of TiO_2 nanopowders. To address the deep gap in the literature, we will conduct a detailed Vickers microhardness analysis of the TiO_2 nanopowders in their different phases. At the same time, the hardness curves enable us to define qualitatively the load-independent hardness parameters in the saturation regions using the various semi-empirical mechanical models. By correlating microhardness data with phase compositions and microstructure, we aim to establish structure–property relationships in TiO_2 nanopowders, essential for tailoring their mechanical properties for applications in coatings, catalysts, and energy storage devices. The combined experimental and theoretical approach adopted will provide a comprehensive understanding of the mechanical behavior of TiO_2 nanopowders. This knowledge will not only fill a significant gap in the existing literature but also contribute to the advancement of TiO_2-based technologies.

2 Materials and methods

2.1 Synthesis of nanosized TiO_2 by sol–gel method

Compared to other synthesis techniques, the sol–gel method is widely preferred for the fabrication of TiO_2 materials due to its numerous advantages, including low processing temperatures, high product homogeneity, cost-effectiveness, and superior efficiency. In this study, TiO_2 nanopowders were synthesized using the conventional sol–gel method, which is based on the hydrolysis and condensation of metal precursors, leading to the formation of metal hydroxides that subsequently transform into nanocrystalline metal oxides. The sol–gel process consists of six fundamental stages: (a) hydrolysis, where metal alkoxides or other precursors react with water to form hydroxyl groups; (b) condensation, which facilitates the formation of metal–oxygen-metal (M–O–M) bonds; (c) polymerization, resulting in the formation of an interconnected gel network; (d) gelation, where a three-dimensional solid network emerges; (e) drying, which removes residual solvents and volatile byproducts; and (f) densification or calcination, where the material undergoes structural consolidation, phase transformation, and crystallization through thermal treatment. These sequential processes enable precise control over the structural, morphological, and physicochemical properties of the synthesized TiO_2 nanopowders, making the sol–gel method an ideal choice for tailoring material characteristics for specific applications.

In the present study, a yellow-colored precursor solution was prepared by adding 17.02 mL of titanium (IV) butoxide ($C_{16}H_{36}O_4Ti$, Sigma-Aldrich) into a beaker, while 67.28 mL of absolute ethanol (C_2H_5OH, Merck) was placed in a separate beaker. The titanium butoxide solution was gradually introduced into the ethanol under continuous and vigorous magnetic stirring for 10 min at room-temperature (RT) to ensure uniform dispersion. Subsequently, while maintaining stirring, 4.8 mL of diethanolamine ($C_4H_{11}NO_2$, Merck) was added dropwise to the mixture, serving as a complexing and stabilizing agent to regulate hydrolysis and condensation reactions. The solution was further stirred in a sealed beaker at a controlled speed of 60 rpm at RT for an additional 1 h to enhance homogeneity and prevent premature precipitation.

In parallel, a secondary solution was prepared in a separate beaker by mixing 10 mL of absolute ethanol with 0.9 mL of distilled water. This secondary solution was then introduced dropwise into the primary titanium precursor solution under continuous stirring to ensure gradual hydrolysis and promote the formation of a stable sol. As the reaction progressed, the solution underwent a sol–gel transition, eventually forming a viscous gel-like structure.

The resulting TiO_2 gel was subjected to a pre-sintering process in a muffle furnace at 300 °C under ambient atmospheric conditions for 30 min. This heat treatment was carried out to facilitate the removal of residual organic solvents and volatile components, thereby increasing the purity of the TiO_2 nanopowder. After these initial heat treatments, the resulting powders, once cooled to room-temperature, were freed from the effects of residual organic substances or phase impurities [32–34]. The powder was then subjected to a mechanical grinding process using an agate mortar for approximately 10 min at RT to achieve uniform particle size distribution and improve homogeneity. The homogenized TiO_2 nanopowder was subsequently heat-treated at a range of annealing temperatures (300, 350, 400, 450, 500, 600, 700, 800, 900, 1000, and 1100 °C) for 1 h in ambient air to induce phase transformations, crystallite growth, and enhanced structural stability. Following thermal processing, the annealed TiO_2 powders were compacted into pellets with a diameter of 10 mm and a thickness of approximately 0.5 mm using a uniaxial pressing technique. Initial compaction attempts at a pressure of 3 metric tons for 3 min resulted in structural failure, including cracking and fragmentation. To improve mechanical integrity and densification, the TiO_2 pellets underwent an additional post-annealing treatment at 300 °C for 1 h. This systematic thermal and mechanical processing approach aimed to optimize the structural, morphological, and phase characteristics of TiO_2 for potential applications in photocatalysis, optoelectronics, and energy-related technologies.

The structural characterization of the synthesized TiO_2 nanopowders was performed using a Bruker D8 Advance powder X-ray diffractometer (XRD) operating at 40 kV and 40 mA. The instrument utilized CuKα radiation with a wavelength of $\lambda = 1.5406$ Å to analyze the crystallographic structure, phase composition, and degree of crystallinity of the samples. Mechanical properties were evaluated through microhardness measurements conducted using a Shimadzu HMV-2 static microhardness tester. The experimentally obtained microhardness values were

systematically compared with theoretical predictions derived from various mechanical models, including Meyer's law, the Proportional Sample Resistance (PSR) model, the Elastic/Plastic Deformation (EPD) model, and the Hays-Kendall (HK) semi-empirical approach. These comparisons aimed to elucidate the deformation mechanisms and hardness characteristics of the samples. The morphological analyses of the samples were carried out using a Quanta FEG 250 scanning electron microscope (SEM). The magnetic properties of the TiO_2 samples were investigated using a Lake Shore 7407 vibrating sample magnetometer (VSM), enabling the assessment of their response to an externally applied magnetic field. Special emphasis was placed on understanding the correlation between magnetic behavior and phase transitions in TiO_2, particularly in relation to the structural modifications induced by varying annealing temperatures. The study aimed to provide a comprehensive understanding of the interrelationship between structural, mechanical, and magnetic properties, thereby contributing to the optimization of TiO_2 samples for potential functional applications.

3 Results and discussion

3.1 XRD analysis

The X-ray diffraction (XRD) patterns of TiO_2 samples annealed at various temperatures are presented in Fig. 1, illustrating the evolution of the crystal structure as a function of annealing temperature due to the thermal reorganization of the semiconductor system. A clear correlation between annealing temperature and crystallization behavior can be observed, particularly in terms of the preferential growth along specific crystallographic directions. At lower annealing temperatures of 300, 350, and 400 °C, the XRD patterns indicate an amorphous structure, characterized by the absence of well-defined diffraction peaks, suggesting an incomplete crystallization process (Fig. 1a). As the annealing temperature increases to 450 and 500 °C, the emergence of sharp diffraction peaks signifies the formation of the anatase phase, a metastable tetragonal polymorph of TiO_2 with nanocrystalline characteristics (Fig. 1a).

A critical phase transition occurs at 600 °C, where the diffraction pattern exhibits peaks corresponding to both anatase and rutile phases (Fig. 1b). This indicates the onset of anatase-to-rutile transformation, a well-documented thermally driven phase transition in TiO_2, where the anatase phase progressively converts into the thermodynamically more stable rutile phase. At this temperature, rutile becomes the dominant phase, while residual anatase peaks persist. Upon further increasing the annealing temperature to 700 °C and above, the anatase peaks completely vanish, confirming the full transformation into the rutile phase (Fig. 1b). The samples annealed at 700, 800, 900, 1000, and 1100 °C exhibit only rutile phase diffraction

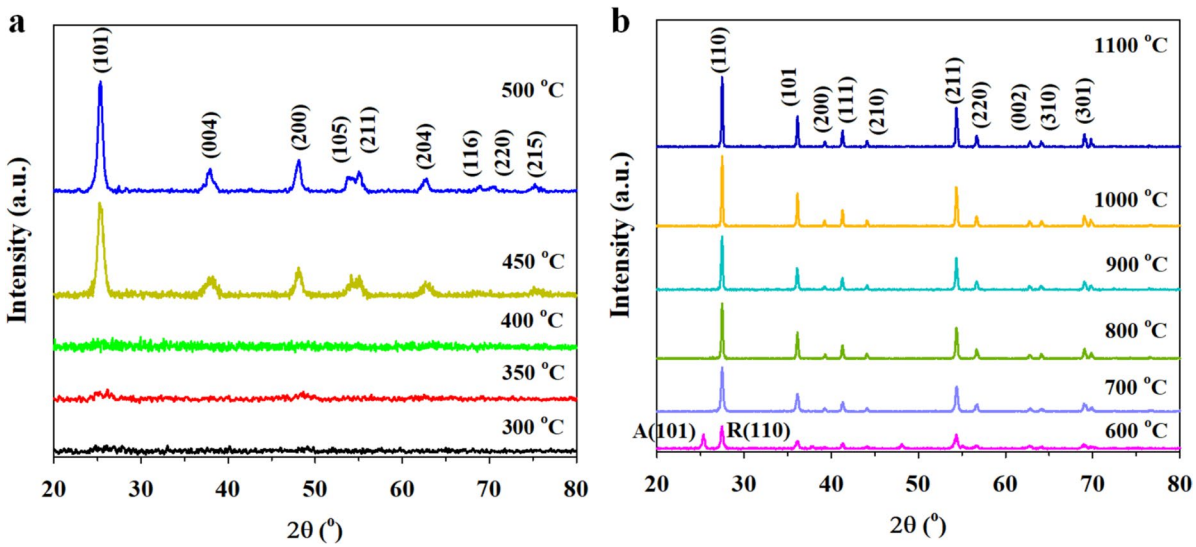

Fig. 1 XRD patterns for TiO_2 nanopowders annealed at **a** 300–500 °C and **b** 600–1100 °C

peaks, signifying the stabilization of the tetragonal rutile structure as the exclusive crystalline phase. This transformation follows the expected thermodynamic pathway of TiO_2, where anatase—a metastable phase at lower temperatures—transitions irreversibly into rutile upon exposure to elevated thermal energy.

Crystallographic analysis reveals that at 450 and 500 °C, the dominant phase is tetragonal anatase TiO_2, corresponding to ICSD reference code 00-021-1272, with space group $I4_1/amd$ (No. 141) and standard lattice parameters a = b = 3.7850 Å, c = 9.4820 Å. The onset of phase transformation at 600 °C is confirmed by the coexistence of anatase and rutile peaks, where rutile begins to dominate. At 700 °C and beyond, complete phase conversion occurs, leading to the exclusive formation of the tetragonal rutile phase, which corresponds to ICSD reference code 00-021-1276, with space group $P4_2/mnm$ (No. 136) and standard lattice parameters a = b = 4.5980 Å, c = 2.9560 Å.

This study highlights the fundamental role of thermal energy as the driving force behind phase transitions in TiO_2. Higher annealing temperatures facilitate the complete stabilization of the rutile phase, offering a practical approach for tailoring the crystal structure of TiO_2 for advanced applications. Furthermore, the primary diffraction peaks of the anatase phase were observed at 2θ values of 25.34°, 37.80°, 48.06°, 53.89°, 55.06°, and 62.69°, corresponding to the (101), (004), (200), (105), (211), and (204) Bragg reflection planes, respectively. In contrast, the main diffraction peaks of the rutile phase appeared at 2θ values of 27.44°, 36.08°, 39.18°, 41.22°, 44.05°, 54.32°, and 56.64°, associated with the (110), (101), (200), (111), (210), (211), and (220) planes, respectively. These results provide critical insights into the structural evolution and phase stability of TiO_2 nanopowders as a function of annealing temperature.

3.1.1 Crystallite size calculation from XRD data

The prepared TiO_2 samples exhibit a nanocrystalline structure, comprised individual crystallites. The crystallite sizes are determined for the samples annealed at temperatures ranging from 500 to 1100 °C using the Debye–Scherrer (D-S) equation (Eq. 1):

$$D = \frac{k\lambda}{\beta \cos\theta} \tag{1}$$

The average crystallite size for the anatase phase, observed in samples annealed at 450 and 500 °C, was determined to be approximately 17 nm. In contrast, the rutile phase, which emerged in samples subjected to annealing temperatures between 700 and 1100 °C, exhibited a progressive increase in average crystallite size, ranging from 29 to 43 nm (Table 1). This observed trend of increasing crystallite size with rising annealing temperature is consistent with the well-established phenomenon of thermally induced grain growth [35].

At elevated temperatures, the thermal energy supplied to the system facilitates atomic diffusion across grain boundaries, enhancing the mobility of atoms and enabling the coalescence of adjacent crystallites into larger grains. This process is thermodynamically driven by the minimization of interfacial energy, leading to a reduction in grain boundary density and an overall coarsening of the microstructure. More specifically, the heat energy accumulated in the intergranular region promotes grain boundary migration, thereby increasing the overall grain size [36].

The results also indicate that higher annealing temperatures contribute to the enhancement of crystallization dynamics and grain boundary coupling within the TiO_2 matrix. This phenomenon is particularly evident from the observed decrease in grain boundary densities, which suggests improved crystallographic

Table 1 Some characterization parameters of TiO_2 nano particles

Samples	a = b (Å)	c (Å)	D-S	$\delta_{hkl}(\times 10^3)$	W–H	
			D (nm)		D (nm)	ε ($\times 10^4$)
500	3.78	9.48	16.91	3.495	10.41	− 32.92
600	4.18	4.49	27.58	1.314	26.28	− 1.96
700	4.59	2.95	29.72	1.132	31.48	1.94
800	4.59	2.95	35.25	0.805	38.51	2.58
900	4.58	2.96	38.50	0.674	48.92	5.58
1000	4.57	2.96	43.21	0.535	62.15	7.11
1100	4.58	2.96	43.21	0.535	49.25	2.84

ordering and phase stability. Additionally, the variation in average grain size as a function of annealing temperature can be attributed to the quantum confinement effect [37, 38], wherein reduced crystallite dimensions at lower temperatures impose constraints on charge carrier mobility and electronic structure. The data presented in Table 1 provide quantitative evidence supporting these structural transformations in TiO_2 nanopowders, highlighting the critical role of annealing temperature as a key parameter in controlling crystallite size. Since crystallite size directly influences fundamental material properties-such as optical bandgap, electronic behavior, and mechanical stability-understanding its dependence on thermal treatment is essential for optimizing TiO_2-based applications in photocatalysis, optoelectronics, and nanotechnology.

3.1.2 *Williamson-Hall (W–H) analysis of crystallite size and lattice strain*

For materials with crystallite sizes below 100 nm, X-ray diffraction (XRD) peaks exhibit significant broadening, which primarily arises from two fundamental factors: (1) the finite crystallite size and (2) the presence of microstrain within the crystal lattice. The observed peak broadening can be systematically analyzed to estimate both the average crystallite size and the magnitude of lattice strain, providing critical insights into the structural properties of nanomaterials.

A well-established approach for distinguishing the effects of crystallite size and strain on peak broadening is the Williamson–Hall (W–H) analysis. This method assumes a uniform distribution of strain across all crystallographic directions and enables a more precise evaluation of structural parameters. By analyzing the five most prominent diffraction peaks in the XRD pattern, a $\beta_{hkl}\cos\theta$ vs. 4 $\sin\theta$ plot is constructed (Fig. 2a). A linear fit to this plot provides key parameters: the slope of the linear regression corresponds to the strain (ε), while the y-intercept yields an estimate of the crystallite size (Table 1) [39].

Compared to the Debye–Scherrer (D–S) method, which assumes negligible strain and can overestimate crystallite size in strained systems, W–H analysis provides a more reliable determination by explicitly accounting for lattice strain contributions. In the present study, W–H analysis establishes a strong correlation between grain size expansion and lattice strain relaxation. The obtained strain and crystallite size values from W–H analysis, alongside crystallite size values derived from the D–S equation, are summarized in Table 1. The calculated strain values are found to be relatively small, resulting in a close agreement between the crystallite sizes obtained from both methods. This observation suggests that thermal annealing promotes lattice strain relaxation, thereby facilitating crystal growth, as evidenced by the observed increase in nanoparticle size with higher annealing temperatures.

Furthermore, a positive slope in the W–H plot indicates lattice expansion, whereas a negative slope suggests lattice contraction. The progressive narrowing of diffraction peaks with increasing calcination temperature signifies enhanced crystallinity within the TiO_2 matrix. As the annealing temperature is elevated from

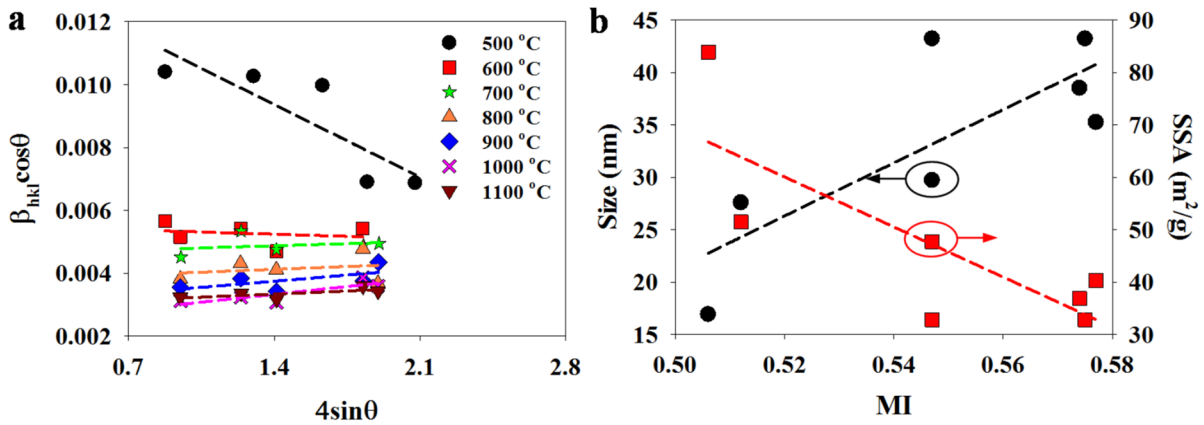

Fig. 2 **a** Williamson-Hall (*W–H*) plot and **b** Morphological index (*MI*) as a function of crystallite size and specific surface area (SSA) for TiO_2 nanoparticles

500 to 1100 °C, a significant increase in grain size is observed, ranging from 16.915 to 43.214 nm (Table 1). This clear trend confirms a direct relationship between grain growth and sintering temperature, reinforcing the role of thermal energy in promoting crystallite coalescence and structural ordering. Additionally, the sharp diffraction peaks observed in the XRD patterns further validate the high crystallinity and phase purity of the synthesized TiO_2 material. Despite noticeable variations in both grain size and lattice strain, the TiO_2 semiconductor maintains its original tetragonal crystal structure, indicating that the thermal treatment does not induce any structural phase transitions beyond the anatase-to-rutile transformation.

3.1.3 The specific surface area (SSA)

Surface characteristics play a crucial role in nanoparticles due to their inherently high surface-to-volume ratio and the variation in crystallite size. The specific surface area (SSA) is a fundamental parameter that quantifies the total surface area per unit mass of a material, directly influencing its chemical reactivity, adsorption capacity, and catalytic performance. As the particle size decreases, both SSA and the surface-to-volume ratio exhibit a significant increase, which enhances surface-dependent phenomena such as surface energy, defect density, and interfacial interactions [40, 41]. Conversely, larger particles display a lower SSA and reduced surface-to-volume ratios, resulting in diminished surface reactivity and altered physicochemical properties.

Mathematically, SSA can be determined using various equivalent formulas, as summarized in Table 2, all of which yield consistent results regardless of the chosen equation. These calculations provide an accurate quantification of SSA, facilitating a comprehensive understanding of the fundamental properties of the studied materials. Moreover, the precise evaluation of SSA is essential for optimizing nanoparticle-based applications in fields such as catalysis, energy storage, photocatalysis, and biomedical engineering, where surface interactions play a dominant role.

$$SSA = \frac{SA_{part}}{V_{part} x Density} \tag{2}$$

$$S = \frac{6x10^3}{D_p.\rho} \tag{3}$$

Both SSA (Specific Surface Area) and S represent the specific surface area of the material, providing a quantitative measure of the total surface area available per unit mass. The parameters V_{part} and SA_{part} correspond to the particle volume and surface area, respectively, while D_p denotes the particle size, and ϱ represents the bulk density of TiO_2, which is 4.23 g/cm^3. As shown in Table 2, both SSA and S exhibit a decreasing trend with increasing annealing temperature. This behavior can be attributed to the thermal-induced grain growth, where elevated temperatures facilitate atomic diffusion and coalescence of smaller crystallites, leading to an overall increase in particle size. Consequently, the reduction in SSA and S suggests a progressive decrease in the total available surface area, a direct outcome of enhanced crystallite stability and densification of the TiO_2 matrix at higher temperatures.

3.1.4 Dislocation density

Dislocation density (δ) is a fundamental parameter that quantifies the total length of dislocation lines per unit volume within a crystalline material.

Table 2 Specific surface area of TiO_2 nano particles

Samples	Size (nm)	Surface Area (nm^2)	Volume (nm^3)	SSA (m^2.g^{-1})	SA to Volume Ratio	MI	δ ($\times 10^{14}$ m^{-2})
500	16.915	48.133	0.135	83.856	354.71	0.506	38.91
600	27.582	17.110	0.078	51.426	217.53	0.512	13.30
700	29.721	12.546	0.062	47.725	201.87	0.547	11.42
800	35.251	10.607	0.062	40.238	170.20	0.577	8.25
900	38.509	9.728	0.062	36.833	155.80	0.574	6.87
1000	43.215	8.627	0.062	32.822	138.84	0.575	5.48
1100	43.214	8.642	0.062	32.823	138.84	0.547	5.38

Dislocations, which are line defects in the crystal lattice, can originate from a variety of factors, including dopant incorporation, mechanical stress, and variations in annealing temperature. These defects have a profound influence on the mechanical, electrical, and optical properties of materials by altering charge carrier mobility, mechanical strength, and structural stability.

The concentration and spatial distribution of dislocations play a critical role in determining the functional behavior of crystalline materials. In a quantitative sense, dislocation density serves as a measure of topological defects, which tend to increase with plastic deformation and thermally induced grain rearrangement. The formation of dislocations requires the activation of specific mechanisms, such as grain boundary migration, homogeneous nucleation, or interactions between lattice imperfections and surface/interface states [42].

In this study, δ was determined using two distinct mathematical formulations, both of which provided closely matching results, thereby confirming the accuracy, reliability, and self-consistency of the calculations. The obtained dislocation density values offer valuable insights into the defect structure of TiO_2 nanoparticles, shedding light on their structural integrity, phase stability, and potential technological applications. Understanding the role of dislocations is crucial for optimizing the mechanical strength, electronic performance, and catalytic efficiency of TiO_2-based materials, particularly in fields such as semiconductor devices, photocatalysis, and energy storage technologies.

$$\delta = \frac{15\beta cos\theta}{4aD} \tag{4}$$

$$\delta = \frac{1}{D^2} \tag{5}$$

The dislocation density (δ) is a crucial parameter that reflects the defect concentration within a crystalline material and directly influences its structural and functional properties. It is mathematically related to diffraction broadening (β), diffraction angle (θ), lattice constant (a), and crystallite size (D). As presented in Table 2, the dislocation density of TiO_2 nanopowders exhibits an inverse correlation with crystallite size, meaning that as the particle size increases, the density of dislocations decreases. This phenomenon can be attributed to the grain growth and lattice relaxation occurring at higher annealing temperatures, where the supplied thermal energy facilitates atomic diffusion, allowing the rearrangement of crystal planes and the reduction of structural imperfections. The decrease in dislocation density indicates an improvement in the crystallinity and phase stability of TiO_2, leading to a more ordered atomic arrangement with fewer lattice distortions. This structural enhancement is particularly beneficial for semiconducting TiO_2 nanoparticles, as higher crystallinity translates to better electronic transport, improved charge carrier mobility, and reduced recombination losses, which are essential for applications in photocatalysis, optoelectronics, and energy storage devices. Therefore, the findings confirm that annealing at elevated temperatures not only stabilizes the tetragonal phase but also enhances the overall material quality by minimizing defects and optimizing structural properties.

3.1.5 Morphology index (MI)

The widespread industrial application of TiO_2 nanopowders is largely attributed to their distinct structural, physical, and chemical properties, including high hardness, well-defined surface characteristics, controlled particle size, and diverse morphological features. To quantitatively assess the morphological attributes of the synthesized TiO_2 nanoparticles, a morphology index (MI) is introduced, which is derived from the full width at half maximum (FWHM) values obtained from X-ray diffraction (XRD) data. The MI is formulated as follows:

$$MI = \frac{FWHM_h}{FWHM_p + FWHM_h}, \tag{6}$$

where MI represents the morphology index, FWHM is the highest FWHM value recorded from the XRD peaks, and FWHM corresponds to the FWHM value of a particular peak of interest. The experimental MI values for TiO_2 samples, as detailed in Table 2, range between 0.50 and 0.56, signifying subtle variations in morphological features as a function of synthesis and thermal treatment conditions.

A key observation from the data are that MI values exhibit a direct correlation with particle size, implying that larger crystallites correspond to higher MI values. Conversely, an inverse relationship is evident between

MI and the specific surface area (SSA), indicating that materials with larger SSA (and thus higher reactivity) tend to exhibit lower MI values. This dual correlation highlights the interdependent nature of morphology, crystallite size, and surface area, which play a crucial role in tuning the functional properties of TiO_2 nanoparticles.

To further quantify and visualize these relationships, curve fitting was applied to the experimental data, and the resulting equation parameters are compiled in Table 2. The fitted curves, as illustrated in Fig. 2b, provide a mathematical representation of the observed trends, enabling the predictive estimation of MI values based on either particle size or SSA measurements. This systematic approach to analyzing morphological parameters allows for a deeper understanding of how the structural and surface characteristics of TiO_2 nanoparticles can be precisely tailored through synthesis methodologies and annealing conditions. Such insights are particularly valuable for optimizing TiO_2-based materials in diverse applications, including photocatalysis, sensors, coatings, and energy storage devices, where morphology-driven performance enhancements are of significant interest.

3.2 Mechanical analysis

In the present study, microhardness experiments were conducted on TiO_2 semiconductor nano particles to systematically evaluate the evolution of fundamental mechanical properties, including Young's modulus (E), brittleness index (B_i), ductility (D), fracture toughness (K_{IC}), and yield strength (Y), under various applied test loads [43]. These mechanical performance parameters are critical in defining the material's response to external forces, providing insight into its deformation behavior and failure mechanisms.

The Vickers microhardness (H_v) of the TiO_2 nanoparticles was determined using the standard indentation method, and the microhardness values were calculated using the following equation:

$$H_v = F/A \approx \frac{1854.4F}{d^2}, \tag{7}$$

where F (N) represents the applied load, and d (μm) corresponds to the average diagonal length of the indentation. The variation of microhardness with applied load is depicted in Fig. 3, revealing a characteristic load-dependent behavior. The microhardness values provide a direct correlation to the material's resistance to localized plastic deformation, serving as a fundamental parameter for evaluating mechanical integrity. Young's modulus (E), a measure of a material's stiffness and resistance to elastic deformation, was estimated using the empirical relation:

$$E = 81{,}9635H_v \tag{8}$$

A higher E value indicates greater rigidity and lower elastic compliance under applied stress. Additionally, the brittleness index (B_i) was calculated to assess the susceptibility of the material to fracture under stress. The brittleness index, defined as the ratio of hardness to fracture toughness, is given by:

$$B_i = H_v/K_{ßc} \tag{9}$$

whereas ductility (D), which describes the extent to which a material can undergo plastic deformation before fracture, is inversely related to B_i:

$$D = 1/B_i \tag{10}$$

Fracture toughness (K_{IC}), which quantifies the material's resistance to crack propagation, was determined using the relationship:

$$K_{ßc} = \sqrt{2E\alpha}, \tag{11}$$

where α represents a material-specific proportionality constant. A higher K_{IC} value signifies improved toughness and a reduced tendency for brittle failure. Yield strength (Y), which defines the stress threshold beyond which permanent plastic deformation occurs, was estimated using:

$$Y \approx H_v/3 \tag{12}$$

All obtained mechanical property values, including H_v, E, Y, K_{IC}, and B_i, are summarized in Table 3. The analysis reveals that as hardness decreases, a concurrent decline in E, Y, and K_{IC} is observed, highlighting the inherent interdependency of these parameters. Notably, the reduction in K_{IC} aligns with the established relationship between fracture toughness and elastic modulus.

A detailed examination of the experimental H_v data reveals a non-linear decrease in microhardness with increasing applied load (F) up to approximately 2.94 N, followed by a plateau beyond 1.5 N. This trend is attributed to the indentation size effect (ISE), which is governed by factors such as the penetration depth of the indenter and the progressive engagement of

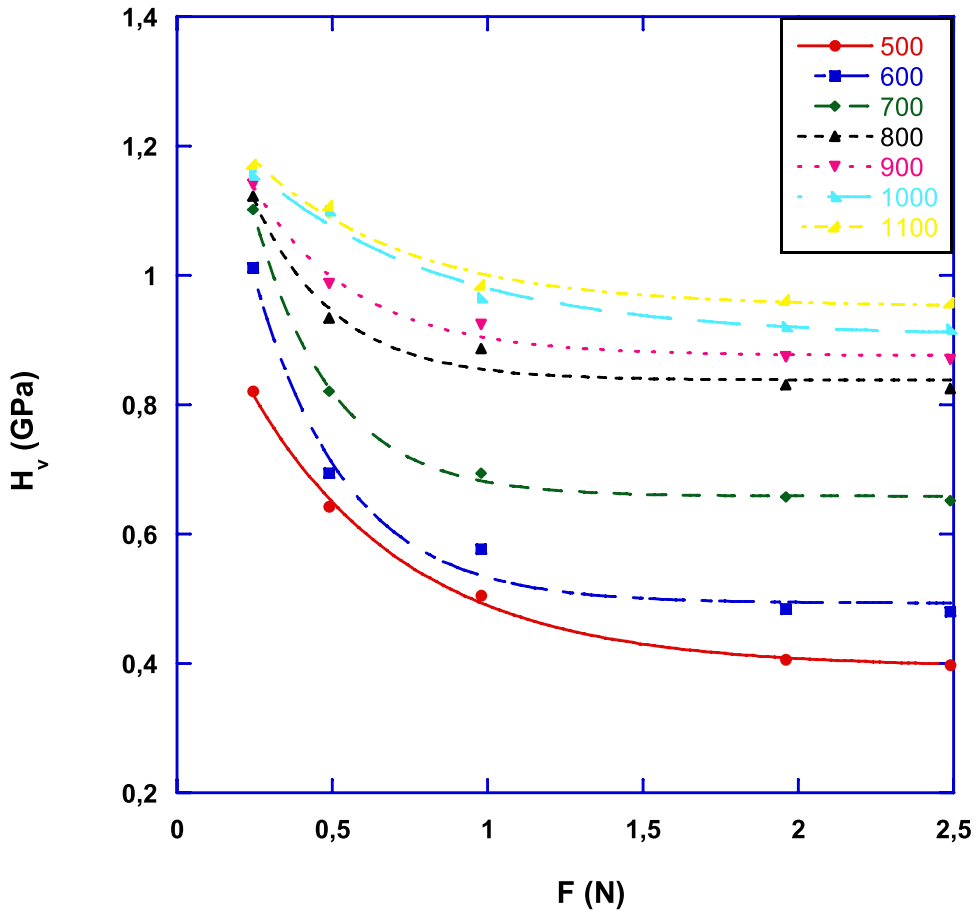

Fig. 3 Vickers microhardness (H_V) as a function of the applied static load (F)

material layers with increasing load. At lower loads, the indenter primarily interacts with the near-surface region, where defects and structural irregularities contribute to higher measured hardness values. Conversely, at higher loads, deeper penetration results in the incorporation of bulk material properties, leading to a stabilization in the hardness response [44].

Furthermore, an increase in microhardness values with annealing temperature was observed, coinciding with the phase transformation from anatase-to-rutile. This finding is in agreement with the well-documented higher hardness of the rutile phase compared to anatase. The enhancement in hardness can be attributed to several factors, including grain growth, improved crystallinity, reduced interparticle boundary defects, and the potential formation of impurity phases that influence mechanical stability.

As the annealing temperature increases (especially beyond 900 °C), a more pronounced increase in hardness values is observed. This may indicate not only a phase transformation but also the formation of a more homogeneous microstructure at higher temperatures. The fact that the rutile phase is more stable at elevated temperatures and exhibits lower diffusion rates may have had a positive effect on microhardness. This can be considered a significant advantage for high-temperature applications. An increase in particle size is expected with increasing annealing temperature. While smaller particles have more grain boundaries, larger crystals contain fewer boundary defects, which partially explains the increase in hardness.

Additionally, the varying densities of different TiO_2 phases can influence microhardness values. There are significant differences in density among anatase, brookite, and rutile phases: anatase has a density of approximately 3.89 g/cm^3, brookite 4.13 g/cm^3, and rutile about 4.25 g/cm^3. These differences arise from variations in atomic arrangement and bonding structure. In particular, the denser and more compact crystal structure of the rutile phase compared to anatase can be associated with higher microhardness values. Such structures generally contain fewer voids and stronger atomic bonds, supporting the hardness increase observed alongside the phase transformation

Table 3 The calculated load-dependent H_v, E, Y, K_{IC}, B_i and D for the samples

Samples	F (N)	H_V (GPa)	E (GPa)	Y (GPa)	K_{IC} (Pa.m$^{1/2}$)	B_i (10^9/m$^{1/2}$)	D (m$^{1/2}$/10^9)
500	0.245	0.821	67.292	0.273	0.991	0.827	1.208
	0.490	0.643	52.702	0.214	0.877	0.732	1.365
	0.980	0.505	41.391	0.168	0.777	0.649	1.540
	1.960	0.406	33.277	0.135	0.697	0.582	1.717
	2.940	0.398	32.621	0.132	0.690	0.576	1.735
600	0.245	1.012	82.947	0.337	1.107	0.913	1.094
	0.490	0.694	56.882	0.231	0.917	0.756	1.322
	0.980	0.577	47.292	0.192	0.836	0.689	1.449
	1.960	0.484	39.670	0.161	0.766	0.631	1.583
	2.940	0.480	39.342	0.160	0.763	0.629	1.589
700	0.245	1.102	90.323	0.367	1.021	1.078	0.927
	0.490	0.821	67.292	0.273	0.881	0.930	1.074
	0.980	0.694	56.882	0.231	0.810	0.855	1.168
	1.960	0.658	53.931	0.2193	0.789	0.833	1.199
	2.940	0.652	53.440	0.217	0.785	0.829	1.205
800	0.245	1.123	92.045	0.374	0.846	1.327	0.753
	0.490	0.934	76.553	0.311	0.771	1.210	0.826
	0.980	0.887	72.701	0.295	0.752	1.179	0.847
	1.960	0.831	68.111	0.277	0.727	1.141	0.875
	2.940	0.825	67.619	0.275	0.725	1.137	0.879
900	0.245	1.141	93.520	0.380	0.840	1.356	0.736
	0.490	0.988	80.979	0.329	0.782	1.262	0.791
	0.980	0.924	75.734	0.308	0.756	1.221	0.818
	1.960	0.874	71.636	0.291	0.735	1.187	0.842
	2.940	0.870	71.308	0.290	0.734	1.184	0.843
1000	0.245	1.155	94.667	0.385	0.865	1.333	0.749
	0.490	1.100	90.159	0.366	0.845	1.301	0.768
	0.980	0.965	79.094	0.321	0.791	1.219	0.820
	1.960	0.921	75.488	0.307	0.773	1.191	0.839
	2.940	0.917	75.160	0.305	0.771	1.188	0.841
1100	0.245	1.172	96.061	0.390	0.802	1.460	0.684
	0.490	1.108	90.815	0.369	0.780	1.420	0.704
	0.980	0.985	80.734	0.328	0.735	1.339	0.746
	1.960	0.962	78.848	0.320	0.726	1.323	0.755
	2.940	0.958	78.521	0.319	0.725	1.320	0.757

during annealing. During transitions to denser phases, particles become more tightly packed, reducing the porosity of the material; as a result, more compact structures with lower porosity are formed, leading to increased measured hardness values. Moreover, not only density but also crystal growth, degree of crystallinity, and reduction in grain boundary defects contribute to hardness. As the annealing temperature increases, the impact of these structural developments becomes more evident. Therefore, when evaluating changes in microhardness, both phase transitions and the overall evolution of the crystal structure should be taken into consideration.

The microhardness measurements were analyzed using multiple theoretical models to comprehensively interpret the indentation behavior of TiO_2 nanoparticles. Meyer's law, which describes the fundamental relationship between applied load and indentation size, was employed to examine indentation size effects (ISE) and reverse indentation size effects (RISE). The Hays–Kendall (HK) model provided insights into load-independent hardness, offering a refined

understanding of plastic deformation mechanisms. Additionally, the elastic/plastic deformation (EPD) model was utilized to evaluate the interplay between elastic and plastic contributions to the indentation process, allowing for a more precise determination of Young's modulus and yield strength [45]. Lastly, the proportional specimen resistance (PSR) model was applied to account for the material's resistance to indentation, serving as a valuable tool for the assessment of load-independent hardness and intrinsic material properties.

This comprehensive mechanical analysis highlights the role of annealing temperature and phase transitions in modulating the hardness, strength, and toughness of TiO_2 nano particles, thereby providing crucial insights into their potential applications in structural, electronic, and optoelectronic fields.

3.2.1 Meyer's law

Meyer's law [46] elucidates the relationship between the applied load (F) and the indentation diagonal length (d) to investigate the ISE phenomenon. This law provides a fundamental framework for analyzing the load-dependent variation in mechanical behavior and is expressed as follows:

$$F = Ad^n, \tag{13}$$

where A is a material-dependent constant representing the force per unit indentation, and n (Meyer's index) characterizes the deformation behavior of the material. Meyer's index is a critical parameter that defines the plasticity and hardness variation during indentation. When $n < 2$, the rate of increase in F is lower than that of d^2, leading to a decrease in the H_v value with increasing load, which signifies the presence of ISE. Conversely, when $n > 2$, the rate of increase in F surpasses that of d^2, resulting in an increase in H_v with increasing applied load. This behavior is referred to as the RISE.

The determination of Meyer's index is conducted by plotting the natural logarithm of the applied load (F) against the natural logarithm of the indentation diagonal length (d), as illustrated in Fig. 4a. To further quantify this relationship, curve fitting is performed on the data, and the obtained equation parameters, including the Meyer index, are presented in Table 4. The fitted curve provides a mathematical representation of Meyer's law, describing the correlation between applied load and indentation size. The Meyer index serves as a crucial metric for understanding the deformation behavior of the material, with $n < 2$ confirming the existence of ISE, as evident from the values in Table 4.

This analysis contributes to a deeper understanding of the impact of thermal processing conditions on the mechanical properties of TiO_2. By determining the Meyer index, it is possible to investigate how phase transitions, grain size variations, and crystal structure defects influence the hardness-deformation relationship. Furthermore, this approach enables a more comprehensive interpretation of plastic deformation mechanisms and their dependence on material microstructure.

3.2.2 Hays-Kendall approach (HK)

This theoretical approach suggests that the minimum applied load (W) required to initiate a visible indentation corresponds to the threshold at which no measurable indentation is observed [47]. The relationship between the applied load (F) and the indentation diagonal length (d) can be expressed mathematically as:

$$F = A_1 d^2 + W, \tag{14}$$

where A_1 is a material-dependent coefficient related to the apparent microhardness, and W represents the minimum threshold load necessary to initiate plastic deformation. The value of W can be extracted from the y-intercept of the linear plot of F vs d^2, as illustrated in Fig. 4b. The experimentally determined W values for the studied TiO_2 samples are listed in Table 4. To ensure the reliability of the data, a curve-fitting procedure was employed, and the resulting equation parameters, including A_1 and W, are presented in Table 4. The Hays–Kendall (HK) model accounts for the load-independent hardness by incorporating this threshold load correction. Consequently, the corrected HK microhardness is computed using the modified load parameter as follows:

$$H_{HK} = 1854.4 \times \frac{F - W}{d^2} \tag{15}$$

This correction provides a more accurate assessment of the intrinsic hardness of the TiO_2 nanoparticles by minimizing the effects of elastic recovery and ISE. By refining the conventional microhardness measurements, the HK approach enhances the

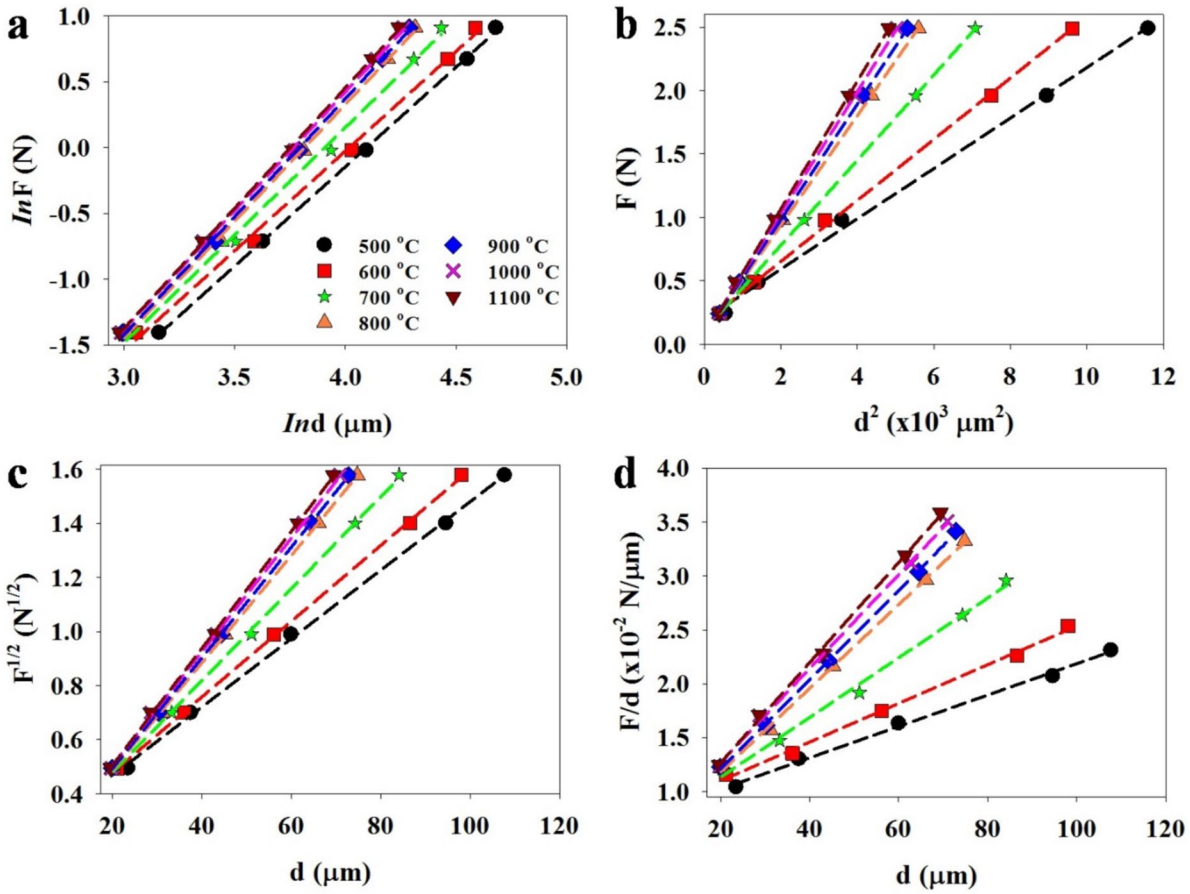

Fig. 4 Plots for analyzing microhardness of TiO_2 nano samples using various models: **a** Meyer's law (*ln(F)* vs. *ln(d)*), **b** Hays-Kendall (H–K) approach (*F* vs. d^2), **c** Elastic/Plastic Deformation (EPD) model ($F^{1/2}$ vs. *d*), and **d** Proportional Sample Resistance (PSR) model (*F/d* vs. *d*)

Table 4 Fitting parameters obtained from the theoretical models for the TiO_2 samples

Samples	Meyer		HK		EPD		PSR	
	n	*InA*	W (N)	A_1 ($\times 10^4$ N/μm^2)	A_2 ($\times 10^2$ N/μm^2)	d_0 (μm)	α ($\times 10^3$ N/μm)	β ($\times 10^4$ N/μm^2)
500	1.51	−6.19	0.195	1.98	1.26	16.90	7.31	1.45
600	1.51	−6.09	0.170	2.41	1.40	14.07	7.40	1.79
700	1.63	−6.39	0.109	3.35	1.69	8.16	5.78	2.77
800	1.77	−6.77	0.076	4.31	1.98	4.49	3.89	4.00
900	1.79	−6.81	0.070	4.55	2.04	4.01	3.78	4.14
1000	1.80	−6.79	0.074	4.79	2.09	4.01	3.96	4.36
1100	1.82	−6.86	0.059	5.03	2.16	3.24	3.35	4.65

understanding of mechanical properties, particularly for nanostructured materials where surface effects and grain boundary interactions play a significant role.

3.2.3 *Elastic/plastic deformation model (EPD)*

The Elastic/Plastic Deformation (EPD) model is a valuable approach for characterizing materials that

exhibit ISE behavior [48]. This model accounts for the fact that when an applied load (F) is removed, partial elastic recovery occurs, leading to a slight reduction in the indentation size. Consequently, an elastic contribution must be incorporated into the total indentation size alongside the plastic deformation. The correlation between indentation size and applied load can be mathematically expressed as follows:

$$F = A_2(d + d_0)^2, \tag{16}$$

where d_0 represents the elastic recovery correction factor, which accounts for the reduction in indentation size due to the elastic component of deformation, and A_2 is a material-dependent load-independent constant. The parameters A_2 and d_0 in the EPD model are determined by analyzing the linear relationship between $F^{1/2}$ and d, as illustrated in Fig. 4c. A linear fit was applied to the experimental data, and the corresponding equation parameters are provided in Table S3. In this relationship, the slope of the graph corresponds to A_2, while the y-intercept represents d_0, both of which are summarized in Table 4. Once these parameters are determined, the EPD-based microhardness (H_{EPD}) can be computed using the modified Vickers hardness formula:

$$H_{EPD} = 1854.4 \times \frac{F}{(d + d_0)^2} \tag{17}$$

By integrating the elastic recovery effect into microhardness calculations, the EPD model offers a more accurate estimation of a material's hardness, particularly for nanoscale and microstructured materials where ISE significantly influences mechanical responses. This model provides deeper insight into the balance between plastic and elastic deformation mechanisms, ultimately improving our understanding of the mechanical integrity of TiO_2 and other semiconductor materials.

3.2.4 *Proportional sample resistance model (PSR)*

The Proportional Sample Resistance (PSR) model, originally formulated by Li and Bradt, provides a comprehensive framework for describing the mechanical behavior of materials exhibiting the ISE [49]. This model is particularly useful in analyzing the mechanical response of a wide range of materials, as it accounts for the energy distribution associated with microstructural voids, defects, and residual fracture formations within the specimen. The fundamental equation governing the PSR model is expressed as follows:

$$F = \alpha d + \beta d^2, \tag{18}$$

where α represents the load-dependent parameter that characterizes the evolution of elastic and plastic deformation during indentation, while β is a load-independent constant that corresponds to the intrinsic hardness of the material. A positive value of $\alpha \backslash \text{alpha}\alpha$ signifies the presence of a conventional ISE behavior, indicating that the hardness decreases with increasing applied load.

The values of α and β are determined by plotting F/d as a function of d, as illustrated in Fig. 4d. Curve fitting is applied to the experimental data, and the corresponding equation parameters are summarized in Table 4. Based on these values, the microhardness of the material, as predicted by the PSR model (H_{PSR}), is calculated using the following expression:

$$H_{PSR} = 1854.4 \times \frac{\alpha d + \beta d^2}{d^2} \tag{19}$$

A comparative analysis of microhardness values obtained through different theoretical models and experimental Vickers hardness (H_v) values for TiO_2 nano particles in both anatase and rutile phases is provided in Table 5. Among the models evaluated, the Hays–Kendall (HK) approach demonstrates the closest agreement with experimentally determined hardness values across the range of applied loads, reinforcing its reliability in predicting load-independent hardness.

Furthermore, the results indicate a strong positive correlation between the annealing temperature and

Table 5 The results of load-dependent Vickers microhardness at the plateau region and load-independent hardness values calculated using HK, EPD and PSR models

Samples	H_{HK} (GPa)	H_{EPD} (GPa)	H_{PSR} (GPa)	H_v (Plateau) (GPa)
500	0.367	0.294	0.268	0.398–0.406
600	0.446	0.363	0.331	0.480–0.484
700	0.621	0.529	0.513	0.652–0.658
800	0.799	0.726	0.741	0.825–0.831
900	0.843	0.771	0.767	0.870–0.874
1000	0.888	0.810	0.808	0.917–0.921
1100	0.932	0.865	0.862	0.958–0.962

microhardness. This trend can be attributed to significant microstructural modifications induced by thermal treatment. As the annealing temperature increases, grain coarsening occurs, leading to a reduction in intergranular spacing. The decrease in grain boundary density enhances grain-to-grain contact, thereby increasing the overall surface energy of the material. This elevated surface energy impedes the movement of the indenter during the microhardness test, requiring a greater applied load to achieve the same indentation depth. Consequently, the increased resistance to plastic deformation manifests as an increase in the measured microhardness. The direct relationship between annealing temperature and microhardness, as evidenced by the data presented in Fig. 5, highlights the crucial role of microstructural control in tailoring the mechanical properties of TiO_2-based materials for advanced technological applications.

3.3 SEM analysis

Scanning Electron Microscopy (SEM) analysis was conducted to examine the morphological characteristics and shape evolution of TiO_2 nanopowders synthesized via the sol–gel method and subjected to calcination at different temperatures ranging from 500 to 1100 °C. The SEM micrographs, presented in Fig. 5, reveal a progressive increase in nanoparticle size with increasing calcination temperature, consistent with the anticipated effect of thermal treatment on particle growth and sintering behavior. The observed size enlargement can be attributed to thermally induced particle coalescence and grain boundary migration, which drive the formation of larger agglomerates at elevated temperatures.

Moreover, the SEM images demonstrate a significant improvement in the uniformity of the nanopowder morphology as the calcination temperature rises. At lower temperatures, nanoparticles exhibit relatively distinct boundaries with reduced agglomeration. However, as the temperature increases, the individual particles begin to merge, leading to a more spherical morphology and increased particle clustering. This enhanced agglomeration is primarily driven by intensified surface diffusion, which facilitates particle coalescence, as well as Ostwald ripening, a process in which smaller particles dissolve and redeposit onto larger ones, further contributing to size growth. Additionally, the increased thermal energy enhances atomic mobility, promoting the densification and structural reorganization of the nanoparticles. These effects collectively result in a more homogeneous morphology with a smoother and more compact particle arrangement at higher calcination temperatures [50].

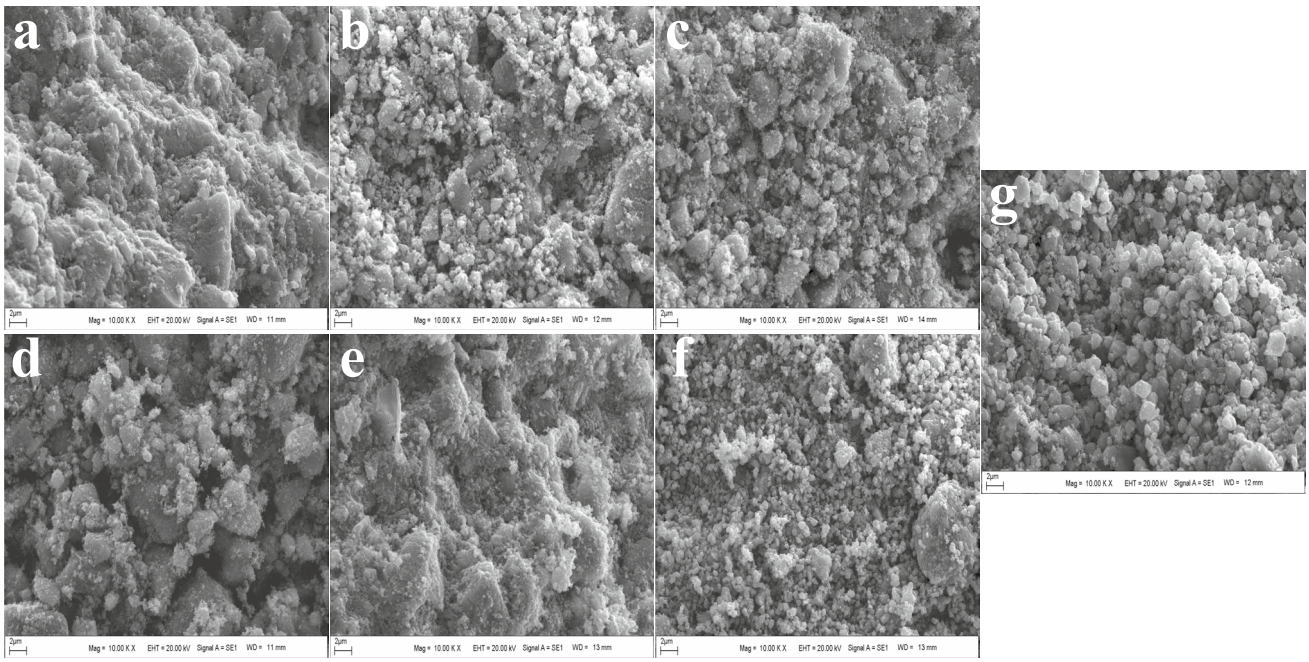

Fig. 5 SEM of TiO_2 samples annealed at **a** 500 °C, **b** 600 °C, **c** 700 °C **d** 800 °C **e** 900 °C **f** 1000 °C, and **g** 1100 °C

3.4 Magnetic analysis

Nanoparticles of metal oxides, including TiO_2, ZnO, CeO_2, SnO_2, Al_2O_3, HfO_2, and In_2O_3, have been widely reported to exhibit room-temperature ferromagnetism (RTFM) [51–53]. However, the precise mechanisms underlying the ferromagnetic behavior of TiO_2 at ambient conditions remain a subject of debate in the literature. Several hypotheses have been proposed to explain the origin of ferromagnetism in TiO_2, including the presence of oxygen vacancy defects [54], lattice distortions [55], titanium vacancies [56], exchange interactions between unpaired spins localized at oxygen vacancies on the nanoparticle surface, and bound magnetic polarons formed due to the interaction of localized electrons with surrounding impurities [57, 58]. These intrinsic and extrinsic defect states play a crucial role in modulating the electronic and magnetic properties of TiO_2 [59, 60].

In this study, magnetization (M–H) measurements were conducted at room-temperature under an applied magnetic field ranging from ± 1.5 T, and the corresponding results are presented in Fig. 6. Key magnetic parameters, including coercivity (H_c), saturation field (H_s), saturation magnetization (M_s), and remanence (M_r), were extracted from the M–H hysteresis loops and summarized in Table 6, with graphical representations provided in Fig. 7. The analysis reveals a strong dependence of TiO_2 nanopowder magnetic properties on annealing temperature. Initially, the H_c value is relatively high at 300 °C, followed by a sharp decrease at 400 °C, and subsequently an increase at 450 °C. Beyond 600 °C, H_c exhibits a relatively low and fluctuating trend. This behavior suggests a transition from dominant superparamagnetic characteristics at lower temperatures to ferromagnetic ordering at temperatures exceeding 500 °C.

Table 6 Magnetization parameters for TiO_2 samples annealed at different temperatures

Samples	H_c (mT)	H_s (mT)	M_s (memu/g)	M_r (memu/g)
300	68.1	173.5	1.94	0.76
350	–	–	–	–
400	4.3	661.0	17.81	0.52
450	58.1	320.3	4.33	1.52
500	6.4	1294.6	19.54	0.80
600	12.2	1391.7	68.40	4.53
700	10.0	1392.0	146.35	7.64
800	9.1	1343.0	81.57	4.65
900	17.9	710.0	29.86	3.60
1000	8.5	1294.3	40.21	2.31
1100	16.3	855.9	27.28	3.29

Examining the evolution of the saturation field (H_s), a lower H_s is observed within the 300–400 °C range, followed by a significant increase at 500 °C. Notably, the H_s value reaches its maximum at 600 °C, coinciding with the anatase-to-rutile phase transition, and subsequently decreases with further temperature increments up to 1100 °C. This suggests a critical role of crystallographic phase transitions in influencing the ferromagnetic response. The variations in M_r and M_s values exhibit a similar trend, with lower values in the 300–400 °C range, a sharp increase at 600–700 °C, and a gradual decline at higher temperatures. These trends imply that

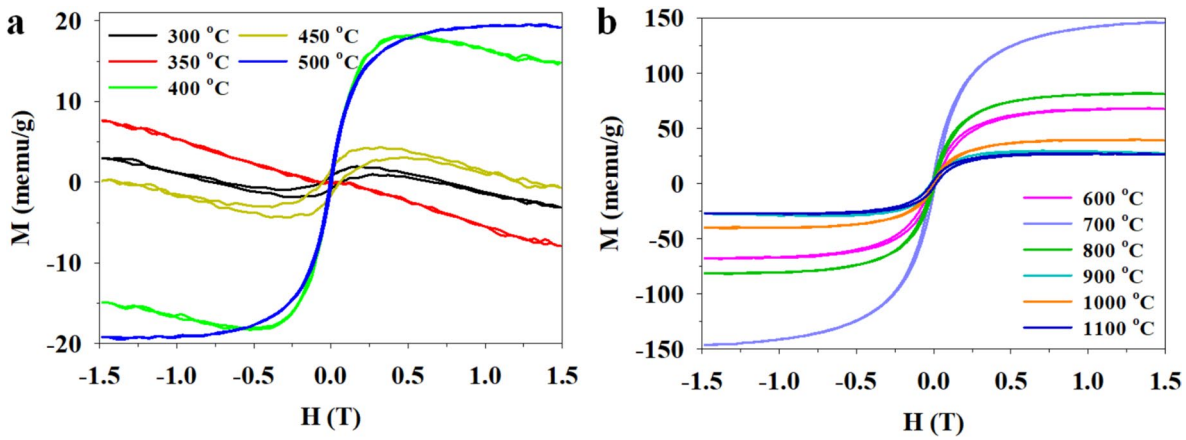

Fig. 6 Magnetization (M) vs applied magnetic field (H) graphs for TiO_2 samples annealed at **a** 300–500 °C and **b** 600–1100 °C

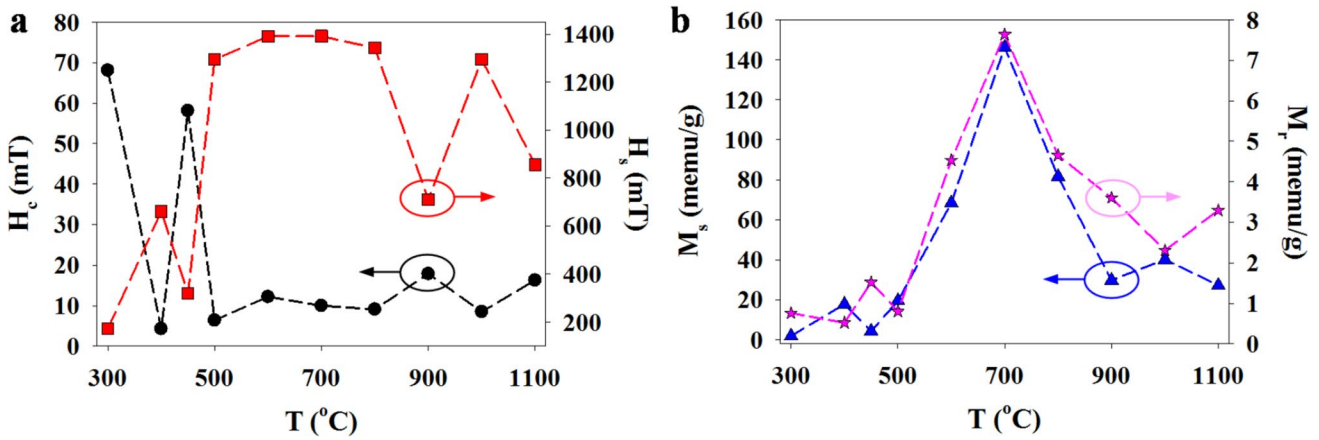

Fig. 7 Magnetic properties of TiO_2 samples as a function of annealing temperature. **a** Coercivity (H_c) and saturation field (H_s), and **b** saturation magnetization (M_s) and retentivity (M_r) as a function of annealing temperature for TiO_2 nanopowders

the overall ferromagnetic response of TiO_2 nanopowders is significantly modulated by thermal treatment.

The emergence of ferromagnetic behavior in undoped TiO_2 is primarily attributed to the presence of oxygen vacancy defects within the crystal lattice. These point defects introduce impurity bands within the semiconductor band structure, effectively acting as electron trap centers. When an oxygen vacancy functions as an F-center, it traps excited electrons, leading to the development of localized magnetic moments and, consequently, weak ferromagnetism. Theoretical and experimental investigations, particularly those conducted by Kim et al. [53], emphasize the role of lattice distortions induced by oxygen vacancies in facilitating room-temperature ferromagnetism, particularly in the rutile phase of TiO_2.

As the annealing temperature increases, enhanced crystallization and grain growth contribute to a reduction in oxygen vacancy concentrations, potentially explaining the observed decline in saturation magnetization at elevated temperatures. This reduction in defect density leads to a weakening of exchange interactions among localized magnetic moments, thereby diminishing the overall ferromagnetic response. However, the complex interplay between structural, electronic, and defect-related mechanisms governing the magnetic properties of TiO_2 nano samples necessitates further in-depth investigations to comprehensively elucidate the underlying physics of room-temperature ferromagnetism in this system.

4 Conclusion

In this study, a systematic investigation was conducted on the structural, mechanical, and magnetic properties of undoped nano-sized TiO_2 synthesized via the sol–gel method and subjected to varying annealing temperatures. X-ray diffraction (XRD) analysis revealed a temperature-dependent phase transformation sequence: amorphous TiO_2 was identified at annealing temperatures of 300, 350, and 400 °C; the anatase phase emerged at 450 and 500 °C; a mixed anatase–rutile phase was observed at 600 °C; and a complete phase transition to rutile occurred at 700 °C and persisted up to 1100 °C. The XRD-derived lattice parameters confirmed that all TiO_2 nano particles crystallized in a tetragonal structure.

To assess the fundamental mechanical properties, Vickers microhardness (H_v) measurements were performed, and the obtained experimental values were compared with those predicted by various theoretical hardness models. Among these, the Hays–Kendall (HK) approximation model exhibited the highest consistency with the experimental data in the saturation region, making it the most reliable model for describing the mechanical response of TiO_2 nano samples.

Scanning electron microscopy (SEM) analysis demonstrated a progressive improvement in particle boundary definition, an increase in sphericity, and enhanced agglomeration as the calcination temperature increased. Additionally, energy-dispersive X-ray spectroscopy (EDX) confirmed the presence of only titanium (Ti) and oxygen (O) in the samples

annealed at temperatures ranging from 500 to 1100 °C, reinforcing the high chemical purity of the synthesized TiO_2 nanoparticles, in agreement with XRD results.

Magnetic characterization, performed via room-temperature magnetization (M–H) measurements under an applied field of ± 1.5 T, revealed that all samples exhibited ferromagnetic behavior with clear magnetic saturation. The weak ferromagnetism observed in undoped TiO_2 is primarily attributed to intrinsic structural defects, particularly oxygen vacancies within the crystal lattice. These defects induce localized magnetic moments, which, through exchange interactions, can facilitate ferromagnetic ordering.

In conclusion, this comprehensive study elucidates the significant influence of annealing temperature on the structural, mechanical, and magnetic properties of sol–gel-derived TiO_2 nanoparticles. The observed phase transformations, microhardness evolution, and temperature-dependent ferromagnetic behavior provide valuable insights into the structure–property relationships of this technologically significant material. These findings contribute to the expanding body of knowledge on TiO_2, further enhancing its potential applications in advanced functional materials, including catalysis, optoelectronics, and spintronic devices.

Acknowledgements

The authors would like to thank the Kastamonu University Scientific Research Projects Coordination Department under the Grant No. KÜBAP-01/2018-19, KÜBAP-01/2022-23, and KÜ-HIZDES/2023-50 and the Kastamonu University Research and Application Center for their supports.

Author contributions

E. Asikuzun Tokeser: conceptualization, writing, and editing; O. Ozturk: writing, reviewing, and methodology, U. Esturk and S. Kurnaz: experimental studies.

Data availability

Not applicable.

Declarations

Competing interests The authors declare that they have no known competing financial interests or personal relationships that could have appeared to influence the work reported in this paper.

References

1. X. Chen, S.S. Mao, Titanium dioxide nanomaterials: synthesis, properties, modifications, and applications. Chem. Rev. **107**, 2891–2959 (2007)
2. G. Yildirim, M. Akdogan, A. Varilci, C. Terzioglu, Role of annealing environment and partial pressure on structure and optical performance of TiO_2 thin films fabricated by RF sputter method. Crystal Research and Technol. **45**(11), 1161–1165 (2010)
3. V. Etacheri, C. Di Valentin, J. Schneider, D. Bahnemann, S.C. Pillai, Visible-light activation of TiO_2 photocatalysts: advances in theory and experiments. J. Photochem. Photobiol. C **25**, 1–29 (2015)
4. B. O'Regan, M. Grätzel, A low-cost, high-efficiency solar cell based on dye-sensitized colloidal TiO_2 films. Nature **353**, 737–740 (1991)
5. K.P. Misra, A. Kumawat, A. Bandopadhyay, B. Modak, S.K. Mukherjee, P.D. Babu, S. Kabi, S. Chattopadhyay, R.D.K. Misra, Structural analysis and magnetic properties of cobalt-doped nanotitania. Mater. Sci. Eng. B **282**, 115761 (2022)
6. A. Mills, S. Le Hunte, An overview of semiconductor photocatalysis. J. Photochem. Photobiol. A Chem. **108**(1), 1–35 (1997)
7. G. Yildirim, S. Bal, M. Gulen, A. Varilci, E. Budak, M. Akdogan, Substrate effect on microstructure and optical performance of sputter-deposited TiO_2 thin films. Cryst. Res. Technol. **47**(2), 195–201 (2012)
8. A. Weir, P. Westerhoff, L. Fabricius, K. Hristovski, N. Von Goetz, Titanium dioxide nanoparticles in food and personal care products. Environ. Sci. Technol. **46**(4), 2242–2250 (2012)
9. S. Jafari, B. Mahyad, H. Hashemzadeh, S. Janfaza, T. Gholikhani, L. Tayebi, Biomedical applications of TiO_2 nanostructures: recent advances. Inter. J. Nanomed. **15**, 3447–3470 (2020)
10. A.L. Linsebigler et al., Photocatalysis on TiO2 surfaces: principles, mechanisms, and selected results. Chem. Rev. **95**(3), 735–758 (1995)

11. O. Carp, C.L. Huisman, A. Reller, Photoinduced reactivity of titanium dioxide. Prog. Solid State Chem. **32**(1–2), 33–177 (2004)
12. D.A.H. Hanaor, C.C. Sorrell, Review of the anatase to rutile phase transformation. J. Mater. Sci. **46**(4), 855–874 (2011)
13. H.Y. Park, W. Kim, H. Park, T. Tachikawa, T. Majima, W. Choi, Photocatalytic and photoelectrocatalytic properties of titanium dioxide nanomaterials. J. Phys. Chem. Lett. **11**(1), 242–255 (2020)
14. A. Chanda, K. Rout, M. Vasundhara, S. Ram, J. Singh, Structural and magnetic study of undoped and cobalt doped TiO2 nanoparticles. RSC Adv. **8**, 10939 (2018)
15. Y. Soon-Do, B. Hun-Soo, Y. Yeon-Hum, Characterization and photocatalytic properties of ceramics TiO_2 nanocomposites. Ceram. Int. **41**, 8241–8246 (2015)
16. J. Zha, H. Roggendorf, *Sol-Gel Science: The Physics and Chemistry of Sol-Gel Processing*, vol. 908 (Academic Press, Boston, 1990)
17. A.E. Danks, S.R. Hall, Z. Schnepp, The evolution of 'sol–gel' chemistry as a technique for materials synthesis. Mater. Horiz. **3**(2), 9–112 (2016)
18. L.C. Klein, *Sol-Gel Technology for Thin Films, Fibers, Preforms, Electronics, and Specialty Shapes* (Noyes Publications, Park Ridge, 1988), p.55
19. L.L. Hench, J.K. West, The sol-gel process. Chem. Rev. **90**(1), 33–72 (1990)
20. L.C. Klein, Sol-gel processing of silicates. Annu. Rev. Mater. Sci. **15**, 227–248 (1985)
21. W. Li et al., Size dependence of thermal stability of TiO2 nanoparticles. J. Appl. Phys. **96**(11), 6663–6668 (2004)
22. J. Livage, M. Henry, C. Sanchez, Sol-gel chemistry of transition metal oxides. Prog. Solid State Chem. **18**(4), 259–341 (1988)
23. Y.F. You et al., Structural characterization and optical property of TiO_2 powders prepared by the sol–gel method. Ceram. Int. **40**, 8659–8666 (2014)
24. M. Niederberger, G. Garnweitner, Organic reaction pathways in the nonaqueous synthesis of metal oxide nanoparticles. Chem. Eur. J. **12**(28), 7282–7302 (2006)
25. C. Sanchez, F. Ribot, Design of hybrid organic-inorganic materials synthesized via sol-gel chemistry. New J. Chem. **18**(10), 1007–1047 (1994)
26. J.D. Wright, N.A. Sommerdijk, *Sol-Gel Materials: Chemistry and Applications* (CRC Press, 2001), p.136
27. M. Gulen et al., Role of annealing temperature on microstructural and electro-optical properties of ITO films produced by sputtering. J. Mater. Sci.: Mater. Electron. **24**(2), 467–474 (2013)
28. M.S. Hegde, K. Nagaveni, S. Roy, Synthesis, structure and photocatalytic activity of nano TiO2 and nano $Ti_{1-x}M_xO_2$ (M=Cu, Fe, Pt, Pd, V, W, Ce, Zr). Pramana **65**, 641–645 (2005)
29. A. Mehrizad, P. Gharbani, S. Motameni Tabatabii, Synthesis of nanosized TiO2 powder by Sol-Gel method in acidic conditions. J. Iran. Chem. Res. **2**, 145–149 (2009)
30. N. Venkatachalam, M. Palanichamy, V. Murugesan, Sol–gel preparation and characterization of nanosize TiO_2: Its photocatalytic performance. Mater. Chem. Phys. **104**, 454–459 (2007)
31. A.K. Tripathi et al., Study of structural transformation in TiO_2 nanoparticles and its optical properties. J. Alloy. Compd. **549**, 114–120 (2013)
32. S. Phromma, T. Wutikhun, P. Kasamechonchung, T. Eksangsri, C. Sapcharoenkun, Effect of calcination temperature on photocatalytic activity of synthesized TiO_2 nanoparticles via wet ball milling sol-gel method. Appl. Sci. **10**, 993 (2020)
33. A. Sharma, R.K. Karn, S.K. Pandiyan, Synthesis of TiO_2 nanoparticles by sol-gel method and their characterization. J. Basic Appl. Eng. Res. **1**, 1–5 (2014)
34. Z. Xie, S. Shuang, L. Ma, F. Zhu, X. Liu, Z. Zhang, Annealing effect on the photoelectrochemical and photocatalytic performance of TiO_2 nanorod arrays. RSC Adv. **7**, 51382 (2017)
35. E. Asikuzun et al., Structural and mechanical properties of (Co/Mg) co-doped nano ZnO. Ceram. Int. **41**, 6326–6334 (2015)
36. T. Seydioglu et al., Effect of foreign impurity and growth temperatures on hexagonal structure and fundamental properties of ZnO nanorods. Microsc. Res. Tech. **87**, 2687–2700 (2024)
37. G.L. Tian, H.B. He, J.D. Shao, Magnetic properties of sol-gel derived TiO_2 nanoparticles. Chin. Phys. Lett. **22**, 1787–1789 (2005)
38. Z. Wang et al., Preparation and characterization of TiO_2 nanoparticles by two different precipitation methods. Ceram. Int. **46**, 15333–15341 (2020)
39. E.A. Tokeser, O. Ozturk, Estimation of microstructural parameters by Williamson-Hall, Halder-Wagner, and size–strain plot methods and magnetic properties of (Cu/Mn) co-doped ZnO nanoparticles. J. Mater. Sci.: Mater. Electron. **34**(31), 2075 (2023)
40. P. Jo-Yong et al., Chemical synthesis and characterization of highly oil dispersed MgO nanoparticles. J. Ind. Eng. Chem. **12**, 882–887 (2006)
41. T. Theivasanthi, M. Alagar, Titanium dioxide (TiO_2) nanoparticles XRD analyses: an insight. arXiv preprint arXiv:1307.1091 (2013)

42. H.C. Ling, M.F. Yan, Microhardness measurements on dopant modified superconducting $YBa_2Cu_3O_7$ ceramics. J. Appl. Phys. **64**, 1307 (1988)
43. G. Güdücü et al., Enhanced thermoelectric performance of $W_{18}O_{49}$/ZnO composite for waste heat recovery with induced high weighted mobility. J. Alloy. Compd. **997**, 174838 (2024)
44. O. Ozturk et al., Evolution of fundamental mechanical properties with aliovalent Co/Cu partial substitution and preparation method for Y-123 system. J. Mater. Sci.: Mater. Electron. **35**, 1018 (2024)
45. E. Asikuzun et al., The effect of zinc on the structural, electrical, and mechanical properties of YBCO-123 superconducting nanoparticles prepared by an acetate-based sol-gel process. J. Supercond. Novel Magn. **32**, 3415–3423 (2019)
46. B.R. Lawn, V.R. Howes, Elastic recovery at hardness indentations. J. Mater. Sci. **16**, 2745 (1981)
47. C. Hays, E.G. Kendall, An analysis of Knoop microhardness. Metallography **6**, 275 (1973)
48. S. Mahshid et al., Mixed-phase TiO_2 nanoparticles preparation using sol–gel method. J. Alloy. Compd. **478**, 586–589 (2009)
49. H. Li, R.C. Bradt, The microhardness indentation load/size effect in rutile and cassiterite single crystals. J. Mater. Sci. **28**, 917 (1993)
50. S.D. Yoo et al., Oxygen-defect-induced magnetism to 880 K in semiconducting anatase $TiO_{2-\delta}$ films. J. Phys.: Condens. Matter **18**, 355–361 (2006)
51. N.H. Hong, J. Sakai, N. Poirot, V. Brizé, Ferromagnetism in transition-metal-doped TiO_2 thin films. Phys. Rev. B: Condens. Matter Mater. Phys. **73**, 3–6 (2006)
52. A.K. Rumaiz, B. Ali, A. Ceylan, M. Boggs, T. Beebe, S. Ismat Shah, Experimental studies on vacancy induced ferromagnetism in undoped TiO_2. Solid State Commun. **144**, 334–338 (2007)
53. D. Kim, J. Hong, Y.R. Park, K.J. Kim, The origin of oxygen vacancy induced ferromagnetism in undoped TiO_2. J. Phys. Condens. Mat. **21**, 195405 (2009)
54. S. Wang, L. Pan, J.J. Song, W. Mi, L. Wang, X. Zhang, Titanium-defected undoped anatase TiO_2 with p-type conductivity, room-temperature ferromagnetism, and remarkable photocatalytic performance. J. Am. Chem. Soc. **137**, 2975–2983 (2015)
55. A.K. Rumaiz, B. Ali, A. Ceylan, M. Boggs, T. Beebe, S. Ismat Shah, Experimental studies on vacancy induced ferromagnetism in undoped TiO_2. Solid State Commun. **144**, 334–338 (2007)
56. S. Šegota, L. Ćurković, D. Ljubas, V. Svetličić, I. Fiamengo Houra, N. Tomašić, Synthesis, characterization and photocatalytic properties of sol-gel TiO_2 films. Ceram. Int. **37**, 1153–1160 (2011)
57. J. Tian, H. Gao, H. Kong, P. Yang, W. Zhang, J. Chu, Influence of transition metal doping on the structural, optical, and magnetic properties of TiO_2 films deposited on Si substrates by a sol–gel process. Nanoscale Res. Lett. **8**, 533 (2013)
58. S.K.S. Patel, N.S. Gajbhiye, Room temperature magnetic properties of Cu-doped titanate, TiO_2(B) and anatase nanorods synthesized by hydrothermal method. Mater. Chem. Phys. **132**, 175–179 (2012)
59. M.V. Adigamova, I.V. Malyshev, I.V. Lukiyanchuk, I.A. Tkachenko, A novel approach to obtaining $LaMnO_3/TiO_2$/Ti composites: features of plasma electrolytic formation, composition, and magnetic properties. J. Alloys Compd. **967**, 171675 (2023)
60. A. Kumari et al., Effect of annealing temperature on the structural, electronic and magnetic properties of Co doped TiO_2 nanoparticles: An investigation by synchrotron-based experimental techniques. J. Alloys Compd. **933**, 167739 (2023)